Applied Catalysis B: Environmental 280 (2021) 119449

Contents lists available at ScienceDirect

Applied Catalysis B: Environmental

journal homepage: www.elsevier.com/locate/apcatb

The superior hydrothermal stability of Pd/SSZ-39 in low temperature passive NOx adsorption (PNA) and methane combustion

Konstantin Khivantsev[a,1], Nicholas R. Jaegers[a,b,1], Libor Kovarik[a,1], Meng Wang[a,1], Jian Zhi Hu[a,1], Yong Wang[a,b,1], Miroslaw A. Derewinski[a,c,1], János Szanyi[a,*,1]

[a] Institute for Integrated Catalysis, Pacific Northwest National Laboratory, Richland, WA, 99352, United States
[b] Voiland School of Chemical Engineering and Bioengineering, Washington State University, Pullman, Washington, 99163, United States
[c] Jerzy Haber Institute of Catalysis and Surface Chemistry, Polish Academy of Sciences, Krakow, Poland

ARTICLE INFO

Keywords:
Palladium
Zeolite SSZ-39
Passive NOx adsorber (PNA)
Methane combustion

ABSTRACT

Uniform SSZ-39 (Si/Al ratio ~12) crystals with an average size of about one micron were synthesized and used to support Pd (0.7–3 wt%) for PNA. The as-synthesized materials were characterized by FTIR, XRD, Helium Ion Microscopy, HAADF-STEM imaging, ^{27}Al, ^{29}Si, and ^{1}H-^{29}Si CP solid state NMR spectroscopic techniques. FTIR studies with CO and NO probe molecules reveal that the majority of Pd is dispersed as isolated Pd(II) and Pd(II)−OH centers and as such is suitable as a low-temperature passive NOx adsorber. Pd(II)-NO, Pd(II)(OH)(NO), and Pd(II)(CO)(NO) complexes form in this material during PNA. Comparison to Pd/SSZ-13 (Si/Al ~12) shows the superior hydrothermal stability of this new material, surviving hydrothermal aging up to 815 °C in 10 % H_2O/Air for 16 h without a significant loss of activity. The SSZ-39 crystal structure remains intact during hydrothermal aging up to 1000 °C confirmed by XRD and HAADF-STEM imaging/EDS mapping. However, changes to the framework, as evidenced by high-field ^{27}Al NMR, during such severe hydrothermal treatment significantly alter the NOx release profiles. Besides PNA, this hydrothermally stable material (3 wt% Pd on SSZ-39; Si/Al ~12) can be used as a robust methane combustion catalyst under practically relevant conditions (i.e., GHSV ~300 L/g*hr). This catalyst shows minimal deactivation after both hydrothermal aging at 750 and 800 °C and prolonged time on stream (105 h) at 425°C. In contrast, both 3 wt% Pd/alumina and 3 wt% Pd/SSZ-13 lose a significant portion of their activity under such conditions, marking an improvement over current technology.

1. Introduction

Pd-containing catalysts and adsorber materials are widely used in various vehicle emission control applications. Indeed, the need to remove extremely toxic NOx from internal combustion engine exhaust is of utmost importance to achieve cleaner air. The ammonia selective catalytic reduction (SCR) technology successfully removes NOx [1,2] at temperatures above 200 °C, with copper ions dispersed in small-pore SSZ-13 zeolite being the catalytically active species. However, at lower temperatures (< 150 °C) no known catalysts are active for this challenging reaction under practical conditions. Moreover, ammonia cannot be dosed successfully onto the catalyst at temperatures < 180 °C when urea is used as the source of NH_3. In order to circumvent this challenge, a very effective passive NOx adsorber material based on Pd/zeolites was introduced by Johnson Matthey, and subsequently explored by other groups [3–11,39–46]. As we have recently shown, the active NOx adsorption sites in these Pd-containing materials are isolated Pd(II) ions dispersed in the micropores of H-SSZ-13 and H-BEA zeolites [5,8,4–11]. We produced high loadings of atomically dispersed Pd in SSZ-13 (Si/Al ~ 6) with the major form of Pd being Pd(II)/2Al sites [8,10,11]. These exhibit excellent performance under dry conditions due to the formation of Pd(I)-NO and Pd(II)-NO complexes as well as nitrosonium (or alternatively nitrosyl) ions in cation exchange positions of zeolites. In the practically relevant wet exhaust streams at low temperatures water readily poisons the coordinatively unsaturated Pd sites [5,9]. However, CO, which is always present in the exhaust stream has a beneficial effect on PNA performance due to the formation of a mixed carbonyl nitrosyl Pd(II)(CO)(NO) complex in SSZ-13 and BEA micropores, thereby mitigating the water poisoning effect [5,8,10]. Although CO was suggested to operate as a reductant to Pd(I), we do not have any evidence that Pd(II) is reduced to Pd(I) by CO. In fact, CO can only directly reduce some Pd(II) cations (most likely in the form of Pd(II)−OH) to Pd(0) clusters,

* Corresponding author.
E-mail address: janos.szanyi@pnnl.gov (J. Szanyi).
[1] These authors contributed equally.

https://doi.org/10.1016/j.apcatb.2020.119449
Received 24 May 2020; Received in revised form 12 August 2020; Accepted 14 August 2020
Available online 20 August 2020
0926-3373/

and not to Pd(I). Pd(II)/2Al sites with naked Pd(II) ions do not have the capacity to be reduced by CO, only H-containing species can reduce them. Pd(II) − OH sites can be reduced by CO via the following scheme: Pd(II) − OH + CO → Pd(II)(OH)(CO) → Pd(II) − COOH → CO_2 + Pd(I) + ½ H_2 or the last step could be as follows: $_{zeolite}$O-Pd(II) − COOH → $_{zeolite}$OH + CO_2 + Pd(0). The released hydrogen can reduce Pd(I) and other Pd cations. Recently, we have discovered [43] that for Pd/FER systems in the presence of CO amounts > 500 ppm during PNA, during heating from low temperature to high temperature, exothermic CO oxidation creates local ("nano") hot spots (that are not picked up easily by thermocouples): heat released during this process was shown to reduce a small amount of Pd cations during each PNA cycle to metallic Pd. Such Pd reduction in Pd/FER was not observed for low CO amounts, only when CO amounts were > 500 ppm. The reduction effect found to be largely reversible upon heating in the presence of oxygen above > 400 ^{0}C due to reoxidation and re-dispersion of small Pd clusters [43].

The role of the Pd(II)(NO)(CO) complex for the PNA performance was recently confirmed for Pd ions on a tungstated zirconia support [12]. Only NO in a dry, oxygen-free stream is able to reduce Pd(II) to Pd (I) via the following reaction: Pd(II) + NO → Pd(I) + NO^+ [11]. As Pd (II)/SSZ-13 was exposed to pulses of NO the initially formed Pd(II)-NO was transformed to Pd(I) and NO^+. This chemistry is analogous to the formation of Cu(I)-NO^+, in which NO is bound side-on to Cu(I) ions [13].

Introducing high loadings of atomically dispersed Pd into zeolites has been a great challenge. Pd is an expensive metal and if it forms PdO nanoparticles outside of the zeolite or inside the pores, its utilization efficiency goes down. We developed a simple, inexpensive method that allowed the syntheses of Pd/SSZ-13 (Si/Al = 6) PNAs with 1.9 (~100 % Pd atomically dispersed) and 3 wt% Pd loadings (90 % atomically dispersed) [8]. These materials show excellent stability after hydrothermal aging, losing only 10–15 % of atomically dispersed Pd due to hydrolysis and Al elution after 16 h of aging in a water/air stream at 750 °C [10]. The thus-formed PdO nanoparticles cannot be easily re-dispersed to their ionic state using gas treatment (oxygen, as well as oxygen + NOx) methods. Pd/SSZ-13 PNA materials we have previously prepared and studied in details lose most of their performance after aging at 800 °C. To date none of the Pd-loaded zeolite materials tested has survived hydrothermal aging to 800 °C while maintaining good PNA performance. Only very recently Pd/FER materials were shown to be hydrothermally stable at 800 ^{0}C without loss of PNA performance [43].

In this study, we report on a Pd/SSZ-39 material that can survive prolonged HTA at 815 °C without losing substantial activity. Nanocrystalline SSZ-39 zeolite ion exchanged with copper has been shown to retain good performance in SCR of NOx after harsh hydrothermal aging at 750 °C [14]. The key to the stability of such system was attributed to the hydrothermal stability of nanocrystalline SSZ-39 [14]. SSZ-13 and SSZ-39 have the same building units and similar framework density, with SSZ-39 apparently showing superior stability to SSZ-13 for SCR applications. With optimized synthesis procedure we produced uniform, approximately micron-sized SSZ-39 crystals with low amounts of high-index facets [15]. The larger, more well-facet-defined crystals are expected to be more stable than their nanocrystalline analogues [9]. Indeed, the crystals we prepared show unprecedented stability after hydrothermal aging with 10 % H_2O/Air flow at 1000 °C with no extensive loss of crystallinity.

The active sites of 0.7 wt% Pd/SSZ-39 (Si/Al ~ 12), similar to that of Pd/SSZ-13 and Pd/BEA, are Pd(II) − OH/1Al and Pd(II)/2Al ions. More specifically, Pd(II)/2Al refers to a palladium +2 ions held as an isolated naked ion near two framework Al atoms (it compensates 2 acidic protons of Si − OH-Al groups). Pd(II) − OH moiety, on the other hand, due to its total charge (+1) requires only 1 framework Al atom to anchor it.

The upper limit of hydrothermal stability of these materials was determined to be above 815 °C in wet streams. Even in the presence of oxygen, ionic Pd in ion-exchange positions becomes unstable and transforms into metallic Pd nanoparticles on the external surface of SSZ-39 (through first hydrolysis into $Pd(OH)_2$) and Pd aluminate. The observed performance deterioration is not due to the collapse of the SSZ-39 framework but to metallic Pd particle formation.

Furthermore, catalytic testing of Pd/SSZ-39 for catalytic methane combustion was also considered. This is an emerging technology used to remove methane from the atmosphere since methane has a 25-fold higher impact as a green-house gas than carbon dioxide (the product of methane combustion). Pd/Alumina is used commonly for methane combustion, but in the wet streams this material shows rapid deterioration due to $Pd(OH)_2$ formation/PdO agglomeration and structural changes to the alumina support [15]. We have previously systematically studied the structure of Pd/SSZ-13 as a function of the Si/Al ratio (from 6 to 30) at a fixed metal loading. The increase in the hydrophobicity of the zeolite framework with increasing Si/Al ratio results in the progressive agglomeration of PdO particles (and concomitant loss of isolated Pd(II) in the zeolite micropores) on the external surface of the zeolite [8]. These guidelines were utilized [16] to produce relatively stable Pd/SSZ-13 methane oxidation catalysts with high Si/Al ratio. Since PdO is imperative for methane oxidation activity, we hypothesized that synthesizing 3 wt% Pd/SSZ-39 (Si/Al ~12) would provide an even more hydrothermally stable methane combustion material. Indeed, we found that this material was remarkably stable, and survived 800 °C hydrothermal aging without significant deactivation for methane combustion. In contrast, Pd/Al_2O_3 and Pd/SSZ-13 both at 3 wt% metal loading deactivated dramatically under the same aging conditions. Moreover, this aged material showed stable long-term performance in methane combustion in practically relevant (wet) gas streams.

2. Experimental methods

Synthesis of SSZ-39 crystals employed the modified synthesis procedure adapted from [17,18], using N,N'-dimethyl-3.5-dimethylpiperidinium hydroxide (DMP) (Sachem Inc.) as structure directing agent (SDA) and FAU zeolite (CBV720 (Si/Al ~ 15) or CBV720 and CBV760 (Si/Al ~ 30) from Zeolyst International) as Si and Al sources.

Modifications of the reported procedures was achieved by varying ageing time, chemical composition of the gel and synthesis time. The applied synthesis method is as follows : first 79.5 g of 20 wt% aqueous solution of DMP was slowly added to solution containing 4.0 g sodium hydroxide (Sigma Aldrich, ≥ 99 %) dissolved in 16.0 g of deionized (DI) water and stirred for 20 min. Subsequently, 33.95 g of FAU zeolite (CBV720, Si/Al = 15) was slowly added (20 min) to the above solution under vigorous stirring. The chemical composition of the gel was SiO_2: 0.033 Al_2O_3:0.20 NaOH :0.20 DMP :9.2 H_2O. The gel was aged under stirring at room temperature for 4 h and transferred into a stainless-steel autoclave with a Teflon liner for 9 days under static conditions (when no FAU impurity was longer detected in the crystalline samples with XRD). The synthesized material was washed with DI water until pH ~ 8.0, washed samples were dried at 90 °C overnight in standard lab furnace and then calcined at 540 °C under flow of dry air (synthetic) at a flow rate of 100 ml/min for 6 h.

Then, to obtain the NH_4-forms from the prepared Na-SSZ-39 zeolite materials, ion-exchange was performed with 1 M aqueous NH_4NO_3 solution at 80 °C for 2 h with intense stirring (under reflux), zeolite/solution = 1:20. Then the ion-exchanged samples were washed with DI water and centrifuged. This procedure was repeated at least 3 times using fresh 1 M NH_4NO_3 solution. The ion-exchanged samples were then dried at 90 °C overnight and calcined at 550 °C overnight in dry air flow. The final Si/Al ratio, based on elemental analysis as well as EDS mapping of the as-made crystals, was approximately ~11 − 12.

Na/SSZ-13 zeolite with Si/Al = 12 was hydrothermally synthesized using the following recipe: 0.8 g of NaOH (Sigma Aldrich, ≥ 99 %) was dissolved in 50 ml of deionized water. Then, 17 g of TMAda-OH (Sachem Inc., 25 % *N,N,N*-trimethyl-1-adamantyl ammonium

hydroxide) was added as structure directing agent. Consequently, 0.75 g of $Al(OH)_3$ (Sigma Aldrich, ~54 % Al_2O_3) was slowly added to the solution and stirred at 400 rpm until it was completely dissolved. Afterwards, 20.0 g of LUDOX HS-30 colloidal silica (Sigma Aldrich, 30 wt% suspension in H_2O) was added slowly to the solution until a uniform white gel was formed. The obtained gel was sealed in a 125 mL Teflon-lined stainless-steel autoclave containing a magnetic stir bar. Hydrothermal synthesis was carried out at 160 °C under continuous gel stirring at 400 rpm for 4 days. After synthesis, the zeolite cake was separated from the suspension by centrifugation and washed three times with deionized water. It was then dried at 80 °C under N_2 flow overnight and calcined in air at 550 °C for 5 h in order to remove the SDA. NH_4/SSZ-13 was obtained by ion exchange of the as-prepared Na/SSZ-13 zeolite with 0.5 M NH_4NO_3 solution at 80 °C for 5 h. The process was repeated three times.

Pd/Zeolite powders were obtained via incipient wetness impregnation with Pd(II) tetra-amine nitrate solution (10 wt%, Sigma) and NH_4-forms of zeolites. The benefits of using palladium (II) tetra-amine nitrate precursor versus palladium nitrate as well as NH_4-forms of zeolite were previously described in detail [10,11,17]. A minimum amount of the Pd(II) precursor solution was added to the zeolite in the amount approximately equivalent to the total pore volume of the zeolite. The thick paste was mixed for 30 min, subsequently dried at 80 °C and calcined at 600 °C in static air., for 5 h (ramping rate 2 °C/min).

3 wt% Pd/Alumina sample was prepared on commercial gamma-alumina (SBA-200, SASOL, ultra-pure) via incipient wetness impregnation, followed by calcination at 600 °C.

Hydrothermal aging (HTA) of Pd/Zeolite and Pd/alumina powders was performed at 750, 800, 815, 900 and 1000 °C for 16 h in a flow reactor with GHSV ~ 150 L/g*hr in a gas mixture containing 10 % H_2O in air.

The in situ transmission IR experiments were conducted in a home-built cell housed in the sample compartment of a Bruker Vertex 80 spectrometer, equipped with an MCT detector and operated at 4 cm^{-1} resolution. The powder sample was pressed onto a tungsten mesh which, in turn, was mounted onto a copper heating assembly attached to a ceramic feedthrough. The sample could be resistively heated, and its temperature was monitored by a thermocouple spot welded onto the top center of the W grid. The cold finger on the glass bulb containing CO was cooled with liquid nitrogen to eliminate any contamination originating from metal carbonyls, while NO was cleaned with multiple freeze–pump–thaw cycles. Prior to spectrum collection, a background with the activated (annealed, reduced or oxidized) sample in the IR beam was collected. Each spectrum reported was obtained by averaging 64 scans.

HAADF-STEM analysis was performed with a FEI Titan 80–300 microscope operated at 300 kV. The instrument is equipped with a CEOS GmbH double-hexapole aberration corrector for the probe-forming lens, which allows for imaging with 0.1 nm resolution in scanning transmission electron microscopy mode (STEM). The images were acquired with a high angle annular dark field (HAADF) detector with inner collection angle set to 52 mrad.

Helium ion microscopy (HIM) images were obtained using 35 keV He ions with 0.1 pA beam current at normal incidence. Secondary electrons were detected using an Everhart–Thornley detector. For HIM imaging, a very thin layer of carbon (< 1 nm) was coated using a carbon sputter deposition system as the samples were completely insulating. The instrument resolution was 0.35 nm. A particle size distribution was obtained by visually measuring and analyzing 100 particles seen in the helium ion micrographs.

^{27}Al MAS NMR measurements were performed at room temperature on a Bruker 600 MHz WB NMR spectrometer, operating at a magnetic field of 14.1 T. The corresponding ^{27}Al Larmor frequency is 156.380234 MHz. All spectra were acquired at a sample spinning rate of 20 kHz (± 5 Hz) and externally referenced to 1.0 M aqueous $Al(NO_3)_3$ (0 ppm). An acquisition time of 100 ms was employed to receive the π/20 pulse width of 0.2 μs which was preceded by a recycle delay of 2 s. Typically, 32,768 scans were acquired to constitute one spectrum.

^{29}Si and ^{1}H-^{29}Si CP MAS solid-state NMR experiments were performed on a Varian-Agilent Inova wide-bore 300 MHz NMR spectrometer and confirmed with a Bruker 600 MHz NMR spectrometer at higher field. ^{29}Si spectra were referenced to tetramethylsilane (TMS at 0 ppm).

Nitrogen adsorption isotherms were measured on Micromeritics ASAP 2020 BET analyzer. Samples were degassed at 300 °C under vacuum for 3 h prior to the measurement. The external surface area was calculated using the t-plot method. Single point adsorption close to $p/p_0 = 0.99$ was used to determine the total pore volume.

X–ray diffraction (XRD) patterns were collected on a Rigaku Mini Flex II bench top X–ray diffractometer using a Cu–Kα radiation of 0.154056 nm (30 kV and 15 mA). Experiments were conducted on a powder sample holder in a 2θ range of 5–60°, with a step size of 0.02°/s. All measurements were performed under ambient conditions.

Standard NOx adsorption tests were conducted in a plug-flow reactor system with powder samples (120 mg, 60–80 mesh) loaded in a quartz tube, using a synthetic gas mixture that contained 200 ppm of NOx or (200 ppm of NOx and 14 % O_2) balanced with N_2 at a flow rate of 210 sccm (corresponding to 220,000 h^{-1}, in which we consider the density of zeolite to be ~2.1 g/cc). All the gas lines were heated to over 100 °C. Concentrations of reactants and products were measured by an online MKS MultiGas 2030 FTIR gas analyzer with a gas cell maintained at 191 °C. Even though it is preferable to use a pure NO feed for the study, the actual NOx feed contained ~190 ppm of NO and ~10 ppm of NO_2, where the latter came from the NO source and background NO oxidation by the heated gas lines. Since realistic engine exhausts do contain ~5% of NO_2 in the total NOx, no effort was made to remove NO_2 from our feed. Two four-way valves were used for gas switching between the reactor and the bypass. Prior to storage testing at 100 °C, the sample was pretreated in 14 % O_2 balanced in N_2 flow for 1 h at 550 °C and cooled to the target temperature in the same feed. The gas mixture was then switched from the reactor to the bypass, and 200 ppm of NOx was added to the mixture. Upon stabilization, the gas mixture was switched back from bypass to the reactor for storage testing for 10 min. The sample was then heated to 600 °C (or any desired temperature) at a rate of 10 °C/min to record the desorption profiles of gases in the effluent.

Standard methane oxidation tests were performed in a plug-flow reactor system with powder samples (60 mg, 60–80 mesh) loaded in a quartz reactor, using a synthetic gas mixture that contained 650 ppm methane, 5% carbon dioxide, 13 % oxygen, 2.6 % water in nitrogen with GHSV ~ 300 L/g*hr. Concentrations of reactants and products were measured by an online MKS MultiGas 2030 FTIR gas analyzer with a gas cell maintained at 191 °C.

3. Results and discussion

3.1. Synthesis of micron-sized SSZ-39 crystals

We optimized the hydrothermal synthesis procedure of Na-SSZ-39 from the synthesis gel with the following composition SiO_2 : $0.033Al_2O_3$: 0.203NaOH : 0.203DMP : $9.2H_2O$. Hydrothermal synthesis was performed under static conditions at 135 − 140 °C for 3–9 days. Analysis of the crystalline products with X-ray diffraction (XRD) revealed that the initial FAU-containing phase completely disappeared after 9 days of hydrothermal synthesis (Fig. S1), leaving only pure phase SSZ-39 (AEI) zeolite. Therefore, this synthesis time (9 days) was enough to produce pure phase SSZ-39 crystals. The sharp peaks in the XRD pattern are indicative of large, uniform crystal size of the as-synthesized material, ~ 1 micron. Nitrogen adsorption isotherms for the two Na-SSZ-39 samples (Fig. S2) from two different batches show 1. similar profiles typical for microporous materials and 2. highly reproducible nature of the designed synthesis. The isotherms for two

different batches of Na-SSZ-39 crystals synthesized in different autoclaves under the same conditions show the same behavior consistent with reproducibility of the synthetic strategy utilized in our work. The obtained isotherm indicates the material is microporous with a micropore volume of 0.3 ml/g and the absence of mesoporosity (perfect crystals) and textural mesoporosity that is present in imperfect crystals and nanocrystals, fully consistent with XRD data. Helium-ion microscopy data further corroborate the combined information obtained from XRD and N_2 adsorption BET data (Fig. S3), i.e., large uniform crystals are obtained via this method.

Calcination and NH_4 ion-exchange have no effect on the crystallinity of the prepared materials (Fig. S4). Moreover, ^{27}Al MAS NMR analysis of template-free i.e. calcined at 540 °C samples showed negligible (~3%) formation of octahedral Al as a result of post-synthesis thermal treatment.

We chose the three-time ion exchange procedure with NH_4NO_3 solution in order to fully exchange sodium ions for ammonium, based on elemental analysis. Moreover, we emphasize that elemental analysis finds Si/Al ratio ~ 12 (not shown) consistent with the ratio inferred from high-field solid-state ^{27}Al and ^{29}Si NMR data [19] (Fig. S5).

In summary, pure SSZ-39 crystals were prepared and extensively characterized. These crystals have high surface area (> 700 m^2/g), low external surface area (2.5−7 m^2/g, from t-plot) and micropore volume of 0.3 ml/g. They were subsequently used to prepare supported Pd/SSZ-39 materials.

3.2. Low-temperature NO_x storage performance of fresh and hydrothermally aged 0.7 wt% Pd/SSZ-39

Applying the method we developed for the preparation of Pd/SSZ-13 [8], we synthesized Pd/SSZ-39 material with Si/Al ~12 and loading of Pd at 0.7 wt%. Previously, we showed that for similar structured zeolite SSZ-13 with Si/Al ~12 nominally 1 wt% Pd/SSZ-13 sample has ~0.8 wt% Pd atomically dispersed and active for PNA; moreover, for Pd/BEA PNA with Si/Al ~12−15 materials we found that progressive decrease of Pd loading from 1 to 0.3 wt% maximizes the amount of atomically dispersed Pd [9]. Thus, we fixed the Pd loading at 0.7 wt% to achieve maximum utilization of expensive Pd and avoid significant formation of PdO nanoparticles inactive for PNA.

Fig. 1 shows NOx trapping followed by temperature-programmed desorption (TPD) of NO_x for the 0.7 wt% Pd/SSZ-39 zeolite (Si/Al~12). During the first 10 min of data recording, the NO_x-containing feed ran through the bypass line while the pre-heated sample (held at 100 °C) was purged with dry N_2. At t = 10 min, the feed was switched to the reactor and kept flowing through the material bed for the rest of data recording. At t = 20 min, we started ramping the temperature to 500 °C at a linear rate of 10 °C/min to desorb the trapped NO_x. The measurement was stopped shortly above 550 °C. Since the NOx inlet concentration was ~200 ppm, in the 10–20 min time-on-stream interval, the negative peaks below 200 ppm represented NO_x storage capacity, and beyond 20 min, the positive peaks above 200 ppm corresponded to NO_x released.

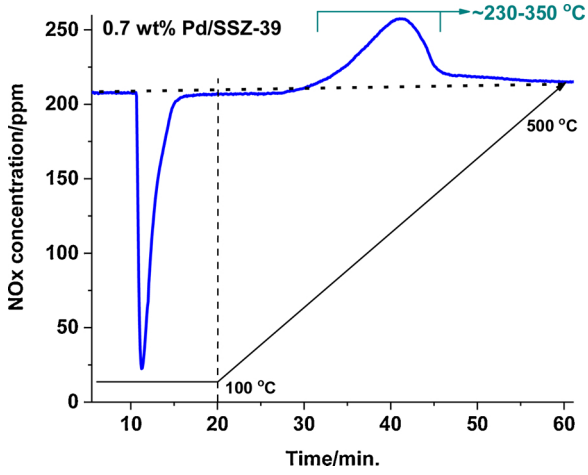

Fig. 1. NOx uptake/release profile of a fresh 0.7 wt% Pd/SSZ-39. NOx adsorption at 100 °C for 10 min followed by TPD (10 °C/min linear ramp rate). Conditions: 120 mg of the sample, ~200 ppm of NOx (190 ppm of NO and 10 ppm of NO_2), 14 % O_2, 200 ppm CO and 2.7 % H_2O balanced with N_2 at a flow rate of 210 sccm. Note that during the first 10 min of data recording, the feed gas runs through a bypass line.

After switching the gas mixture from by-pass to the reactor, the 0.7 wt% Pd/SSZ-39 can store NOx, as it is evidenced by the drop in NOx level from ~200 ppm to < 25 ppm. Due to the low Pd loading, however, no complete NOx removal period was observed during the uptake part of the cycle. The NO_x release is evident between 200 and 350 ^{0}C with a maximum amount NO_x desorption rate at 300 ^{0}C.

Since only isolated Pd ions are active for PNA, the calculated NO/Pd ratio is ~0.9, which means that the majority of Pd (at least 90 %) is dispersed atomically in this sample, consistent with our synthetic method. Moreover, only 1 NO molecule can be adsorbed per 1 Pd atom [8]. Although, for Pd/BEA system we were able to detect the formation of Pd(II)$(NO)_2$ dinitrosyl complex in the presence of NO, these complexes were unstable with respect to temperature as well as under lower partial pressure of NO, and thus did not contribute to the observed PNA performance [9].

Compared with Pd/SSZ-13 (Si/Al ~12), the NOx uptake efficiency measured for the Pd/SSZ-39 is similar, but the temperature of NOx release is different [8] for the two structures highlighting the differences between these two framework structures built using the same D6r building units.

3.3. FTIR spectroscopic investigation on 0.7 wt% Pd/SSZ-39 using NO and CO probe molecules

In order to understand the Pd speciation in Pd/SSZ-39 materials, we performed FTIR measurements on the Pd/SSZ-39 samples (Si/Al = 12). We turned to infrared spectroscopy because it is the most sensitive technique that can provide a clear snapshot of each individual type of Pd species, be it ions or nanoparticles, with CO and NO probe molecules: the infra-red signature of chemisorbed CO and NO is very intense due to their high molar absorption coefficient [20,21]. Furthermore, CO and NO adsorbed on different types of metal cations have distinct spectroscopic signatures [22,23]. For metal/zeolite systems we have previously successfully applied CO adsorption FTIR to characterize Pd (II) and Pt(II) adsorption sites [8,11] and showed the selective formation of Pd(II)(NO)(CO) complexes [5,8,9] as well as changes occurring for Pd/zeolite system during hydrothermal aging [10]. Therefore, it was important to determine which Pd species are present in the 0.7 wt% Pd/SSZ-39 sample. Fig. 2 shows a series of IR spectra collected during sequential CO exposure of the dehydrated Pd/SSZ-39 sample.

Comparing the spectra displayed in Fig. 2 to those obtained from 1 wt% Pd/SSZ-13 (Si/Al = 6) [8,11] striking differences are observed. In our previous study, the majority of Pd (> 95 %) was present as Pd(II) ions held near two proximal Al sites, abbreviated as Pd(II)/2Al (these sites do not necessarily have to belong to the same 6 or 8-membered ring; two Al sites close enough in distance can electrostatically hold extremely electrophilic Pd(II) species in a Pd/2-O-Zeolite charge transfer complex) [8,11]. The band that grows first upon CO adsorption is centered at 2127 cm^{-1}. At higher partial pressures of CO new bands develop: 2211 and 2190 cm^{-1} (belonging to Pd(II)$(CO)_2$ species of Pd (II)/2Al [8,11]) and the 2141 cm^{-1} band. Based on our previous studies supported by DFT calculations [8,11], we assign the 2127 cm^{-1} band to Pd(II)(OH)(CO) complex (or alternatively Pd(II)(CO) complex: we cannot exclude either assignment at present) and the 2140 cm^{-1} band to a different Pd(II)(OH)(CO) complex. New bands growing at higher partial pressures of CO are assigned to polycarbonyl Pd(II) complexes,

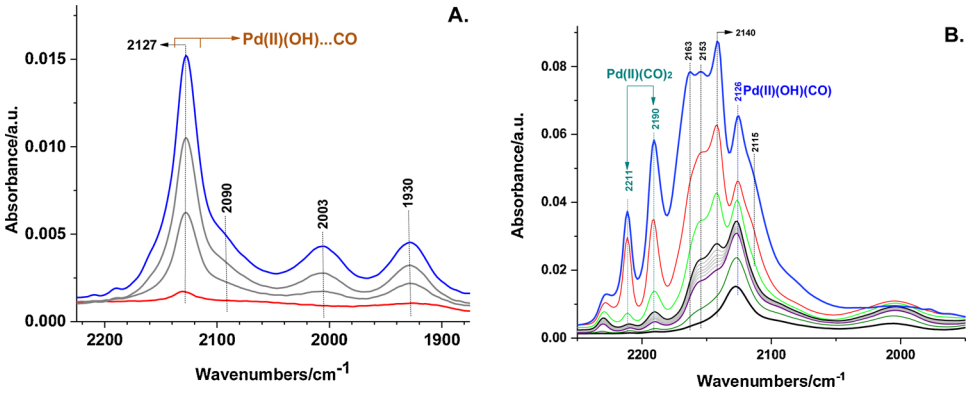

Fig. 2. Series of FTIR spectra collected during sequential CO exposure of the 0.7 wt% Pd/SSZ-39 (Si/Al ~ 12): A: low dose CO ($P_{max.}$ = 0.1 Torr); B: high CO pressure ($P_{max.}$ = 10 Torr). [T_{ads} = 25 ^{0}C].

e.g., $Pd(II)(CO)_3$. The reason for this assigned is as follows: upon evacuation these 3 bands disappear in concert suggesting that they belong to $Pd(II)(CO)_3$ (or $Pd(CO)_x$ where x > 3) species (Fig. S6)

Minor features at 2090 and 2000 cm^{-1} belong to CO adsorbed linearly on Pd nanoparticles and Pd nanoclusters. However, those bands have higher molar extinction coefficients than those representing CO bound to ionic Pd, and thus, are present in small amounts compared to Pd(II) species [11,20]. This result is further corroborated by HAADF-STEM images coupled with EDS mapping (vide infra) and high NO/Pd efficiency. Overall, compared to Pd/SSZ-13, more diverse Pd(II) species are present in the micropores, namely Pd(II) and Pd(II) − OH in different positions, highlighting a more diverse microporous environment of SSZ-39 for loading divalent Pd ions. However, this does not have a detrimental effect on NOx adsorption efficiency, suggesting that various Pd(II) and Pd(II) − OH species are in fact active species for low temperature PNA.

Adsorption of NO (Fig. 3) on the dehydrated 0.7 wt% Pd/SSZ-39 further complements the CO adsorption data. Three absorption features begin to grow simultaneously upon NO adsorption in the 1900 − 1800 cm^{-1} region. The bands in this region belong to NO chemisorbed on cationic Pd sites. We have previously shown that, although, these bands fall in the region typical for linearly adsorbed NO, NO in fact binds with its unpaired electron forming a fully covalent bond with an electron given by Pd(II) [8,13,11]. The formation of the strong covalent Pd-N bond in the bent Pd-N-O fragment is the reason Pd ions in zeolite can function as low-temperature passive NOx adsorbers, i.e., bind NO at 100 ^{0}C and release it above ~200 ^{0}C. Using spectroscopy and DFT, we were able to identify different Pd(II)-NO complexes formed under various gas environments on BEA and SSZ-13 zeolites, including Pd(II) carbonyl-olefin and Pd(II) nitrosyl-olefin species, in addition to Pd(II)-NO, Pd(I)-NO, $Pd(II)(NO)_2$ (which forms only on BEA but not on SSZ-13) and Pd(II)(NO)(CO) (formed on both zeolites) [8–11].

Here, we have a diversity of Pd(II) sites present including Pd(II) and Pd(II) − OH. NO adsorption on Pd(II) − OH leads to the formation of Pd(II)(OH)(NO) complex with NO band at 1810 cm^{-1}. We have previously shown the band around ~1805 cm^{-1} for Pd/SSZ-13 belonged to Pd(I)-NO [8,11]. This band forms due to the ability of NO to reduce Pd(II) with the formation of Pd(I) center and NO^+ anchored on the neighboring O-Al site. Although this transformation has been suggested to take place before, very recently we proved that it indeed takes place spectroscopically for Pd(II)/SSZ-13 under exclusively dry and pure NO: we pulsed NO on Pd(II)/SSZ-13 – as soon as the pressure stabilized with the formation of some specific amount of Pd(II)(NO) (band at 1865 cm^{-1}), we let this equilibrate and then followed the changes in the IR spectra as a function of time. The intensity of 1865 cm^{-1} feature decreased, while the band at ~1805 cm^{-1} of Pd(I)-NO increased in that case. Concomitantly, a different type of species, assigned to NO^+, was formed with the signature at around 2160 cm^{-1} [11]. This is completely analogous to the process of Cu(II) reduction with NO with the formation of Cu(I)-NO^+ fragments, with NO bound side-on in Cu/SSZ-13 [13]. Therefore, it would be tempting to assign the 1810 cm^{-1} band to the Pd(I)-NO complex in Pd/SSZ-39. However, in that case simultaneous formation of NO^+ should have been observed [11,13] which was clearly not the case. Thus, we assign the 1810 cm^{-1} feature to NO bound to Pd(II) − OH species. The two bands at 1879 and 1865 cm^{-1} belong to two different Pd(II)-NO species (located in different crystallographic positions of the zeolite).

After saturation of the sample with NO, we performed subsequent CO adsorption (Fig. 4).

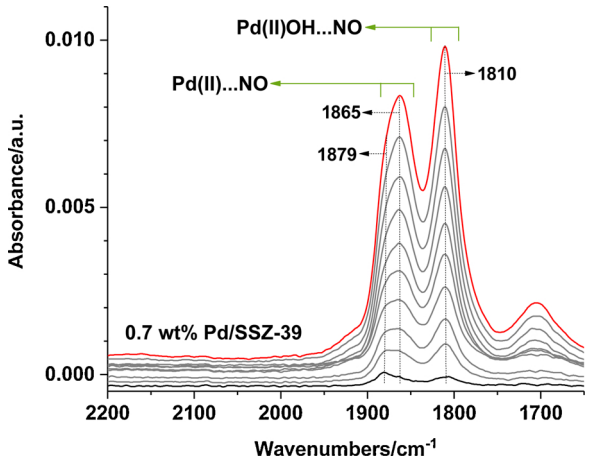

Fig. 3. Series FTIR spectra collected during sequential NO adsorption ($P_{NO,\ max}$ = 5 Torr) on the 0.7 wt% Pd/SSZ-39 sample (Si/Al ~ 12). [T_{ads} = 25 ^{0}C].

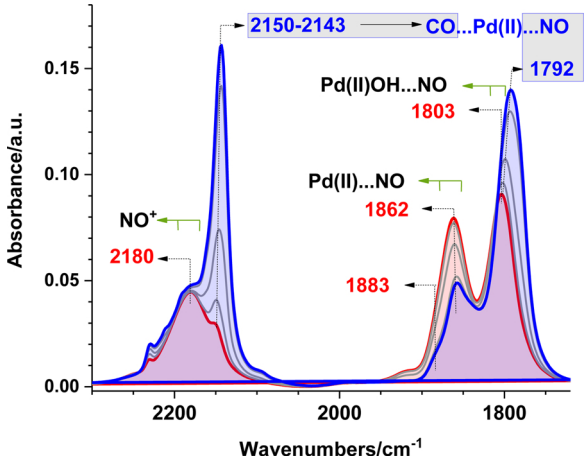

Fig. 4. Series of IR spectra collected during the step-wise exposure of a NO-saturated 0.7 wt% Pd/SSZ-39 (Si/Al ~12) samples to CO (P_{max} = 10 Torr) at 25 ^{0}C.

We have previously shown that Pd(II)-NO in SSZ-13 selectively forms the Pd(II)(CO)(NO) complex upon CO adsorption [8,11] which is largely responsible for the excellent performance of Pd(II)/SSZ-13 as a low temperature passive NOx adsorber (at 100 ^{0}C). However, in this case, we observe the unselective formation of Pd(II)(CO)(NO) even at elevated CO pressures (up to 10 Torr). Clearly, the Pd(II)(OH)(NO) band is not perturbed by the presence of CO, whereas the ~1880 and ~1863 cm^{-1} bands lose a large fraction of their intensities due to the formation of Pd(II)(CO)(NO) mixed ligand complex upon exposure to CO. Thus, under PNA conditions a multitude of species, Pd(II)(OH)(NO), Pd(II)(NO)(CO) and Pd(II)(NO), contribute to the observed adsorption behavior.

3.4. PNA performance of hydrothermally aged Pd/SSZ-39 materials

One of the most important requirements for the materials to be used in automotive after treatment applications is their hydrothermal stability. We have previously showed that Pd/SSZ-13 would survive prolonged (16 h) hydrothermal aging up to 750 ^{0}C in 10 % H_2O, losing only 10–15 % of their NOx storage capacity [10]. This performance loss is related to the agglomeration of isolated Pd(II) into large PdO (most likely through transient formation of mobile hydrated $Pd(OH)_2$ or $PdAl(OH)_x$ species) nanoparticles on the external surface of the zeolite. Such particles cannot be easily re-dispersed back to their single ionic state due to their inherent stability and the concomitant dealumination of the framework upon hydrothermal aging. These processes lead to elution of the framework anchoring paired and mono-Al T sites that are critical for stabilizing Pd(II) and (a minor fraction) Pd(II)−OH. [10]

However, when we aged our best Pd/SSZ-13 material at 800 ^{0}C severe performance loss was observed (~50 %). Therefore, we aged our Pd/SSZ-39 sample which contain different Pd(II) and Pd(II)−OH sites, at different temperatures and evaluated its performance (Fig. 5).

The NOx uptake curves of the samples aged at 750 and 815 °C are similar to those of the fresh sample with high NO/Pd ratio ~0.9 after 750 °C and ~0.8 after 815 °C aging. This means that NOx uptake did not change even after such severe aging and almost all of the Pd ions remain available for adsorption. However, very significant changes are observed in terms of NOx release temperature. The NOx release feature broadens and splits into two peaks: desorption starts above 200 °C and concludes just below 500 °C. This is very different from both Pd/BEA and Pd/SSZ-13 with similar Si/Al ratio and Pd loading: for those samples after aging we observe the increase in the low-temperature release

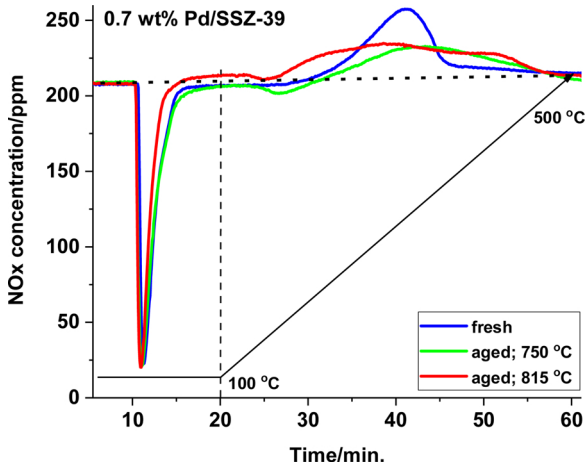

Fig. 5. NOx uptake/release profiles of fresh and aged (750 and 815 °C) Pd/SSZ-39 samples. NOx adsorption at 100 °C for 10 min followed with TPD (10 °C/min linear ramp rate). Conditions: 120 mg of the sample, ~200 ppm of NOx (190 ppm of NO and 10 ppm of NO_2), 14 % O_2, 200 ppm CO and 2.7 % H_2O balanced with N_2 at a flow rate of 210 sccm. Note that during the first 10 min of data recording, the feed gas runs through a bypass line.

feature with the concomitant decrease in the high-temperature NOx release feature [10]. However, here we observe broadening of the NOx release feature without a change in the NOx uptake. This marks the material as the most stable PNA reported so far which survives harsh aging in a 10 % water/air mixture for 16 h at 800 ^{0}C. To the best of our knowledge, no other oxide or zeolite-based PNA material has been shown to survive such harsh conditions. Although, Pd remains atomically dispersed, the changes in the NOx release feature indicate the presence of less homogeneous distribution of Pd(II)-NO sites: the Pd-N bond strength dictates the release temperature, and the broadening of the release event on the temperature scale indicates that a more diverse set of Pd(II)-NO sites evolves [10]. This happens due to electronic changes to Pd because no changes in zeolite crystallinity is observed in XRD (Fig. 7, vide infra). Such changes occur because of the changes in the electronic environment of framework Al sites. We probed these changes in Pd/SSZ-39 with high-field solid state NMR for samples aged at different temperatures. NMR technique has been successfully applied to investigate both Al and other NMR-visible nuclei in various supported materials [24–27,40]. Indeed, we observe significant broadening of the Al T-sites in the 800 °C sample (Fig 13).

The ^{27}Al NMR spectrum of the parent (i.e., NH_4-SSZ-39) zeolite shows the presence of exclusively Al_{tetra} species. Loading the sample with Pd and subsequent calcination at 500 °C result in the formation of a small fraction of Al_{octa} sites. Hydrothermal aging at 800 °C significantly affects the distribution of differently coordinated Al^{3+} ions: 1. the number of octahedral sites increase substantially, 2. the mostly symmetric Al_{tetra} feature broadens, showing the presence of Al_{tetra} ions in at least two differentiable environments and 3. the signal of Al_{penta} ions appear. These changes are even further accentuated in the sample hydrothermally aged at 900 °C where the number of Al^{3+} ions present in octahedral positions (i.e., in extra framework sites) exceed those in tetrahedral sites. Concomitant to the extensive loss of Al_{tetra} sites in the zeolite structure is the dramatic decrease in (~ 85 %) the NOx storage capacity of this sample. (Figs S7).

The performance deterioration of Pd/SSZ-39 at temperatures exceeding 815 °C could stem from either the loss of crystallinity (framework collapse), elution of Pd from the framework or both. A series of XRD patterns collected from the fresh and hydrothermally aged (at different temperatures) SSZ-39 samples (both in NH_4/ and Pd/H form) are displayed in Fig. 7. Strikingly, the 1000 °C aged H/SSZ-39 mostly preserved its crystalline structure, just as the 815 °C aged 0.7 wt% Pd/SSZ-39. Hydrothermal aging of the Pd/SSZ-39 even at 900 °C resulted in only small extent of intensity loss of the diffraction peaks, substantiating the preservation of the crystalline zeolite structure even under these severe aging conditions. These results are fully consistent with those discussed above for the ^{27}Al NMR data (Fig. 6).

To get more insight we performed HAADF-STEM imaging on the fresh and 900 °C aged samples with EDS mapping and collected XRD patterns for the crystals. The HAADF-STEM images of the fresh crystals agree very well with helium ion microscopy images (Fig. S3) and support our conclusion regarding the as-prepared Pd/SSZ-39 materials: large cubic SSZ-39 crystals are formed with regular shapes (Fig. 8).

The material is highly crystalline (Fig. 8A, viewed along [001] projection). Some PdO clusters can be seen on the external surface of SSZ-39 crystals in Fig. 8 C (Pd K-edge map clearly shows the presence of PdO agglomerates on the surface on the bottom edge). EDS mapping of the crystals reveals Si/Al ratio ~11−12, fully consistent with elemental analysis and ^{29}Si NMR data. EDS maps for Si, O, Al, and Pd are displayed in panel C of Fig.8. Homogeneous distribution of Al throughout SSZ-39 crystals is observed. The majority of Pd is present in highly dispersed state (ions), confirmed by EDS mapping and presence of individual Pd atoms viewed along [001] projection (circled in red). Due to the sensitivity of Pd to the electron beam (it easily induces the movement of Pd atoms at 300 keV), assignment of the individual Pd atoms to specific framework locations in the cage system of SSZ-39 (the majority of the Pd can be seen in the *d6r* units), cannot be done with

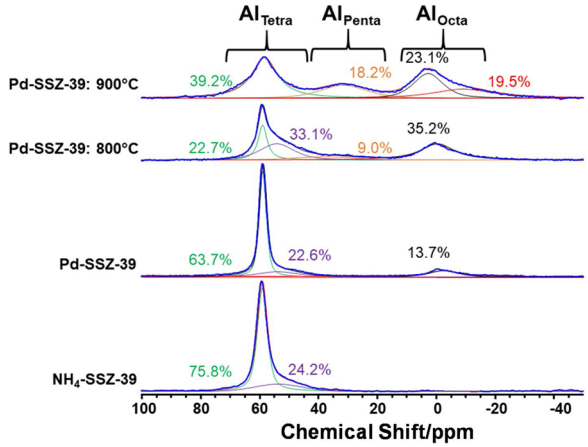

Fig. 6. High-field ^{27}Al MAS-NMR spectra for the fresh (NH_4^+ and 0.7 wt% Pd form) and aged (800 and 900 ^{0}C, 16 h) SSZ-39 samples (Si/Al ~ 12). The site distribution, denoted as Al_{Octa} (for octahedral sites ~ 0 ppm), Al_{Penta} (for penta-coordinated sites ~ 30 ppm) and Al_{Tetra} (for tetrahedral framework Al sites ~ 60 ppm) in percentages are also shown. All spectra are background-subtracted and relative intensities referenced to the fresh sample.

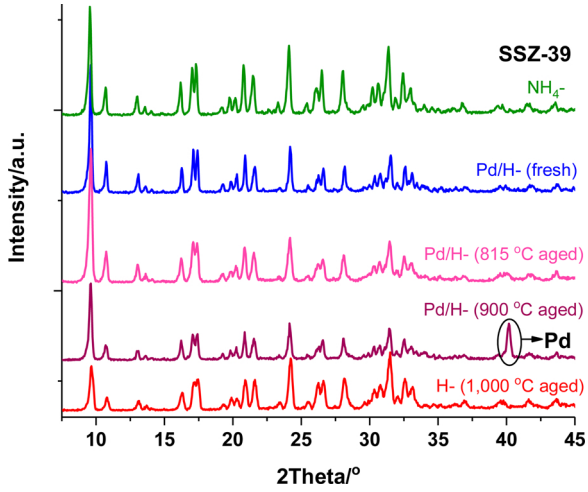

Fig. 7. XRD profile for NH_4-SSZ-39, H/SSZ-39 aged at 1000 °C, and fresh and aged (815 and 900 °C, 16 h) 0.7 wt% Pd/SSZ-39 (Si/Al ~ 12) samples.

confidence.

After 900 °C hydrothermal aging the Pd/SSZ-39 crystallites were imaged again (Fig. 9).

After the 900 °C HTA essentially the same intact crystals with perfect crystallinity were observed, fully consistent with the diffraction patterns shown above. Another important finding from the diffraction pattern is the presence of incommensurate lattice in the SSZ-39 sample (Fig. 9C). (Incommensurate lattice can be described as lattice with a long range periodicity modulation, which is incommensurate with the underlying lattice. That is, the ratio between the periodicities of basic lattice and the modulation is irrational number, Fig. S8). The presence of such lattice has not been previously observed or stated for SSZ-39 (or isostructural zeolites), although, isostructural zeolite SAPO-18, for example, has been studied with electron microscopy [28]. We note that the presence of incommensurate lattice may potentially be one of the factors contributing to such high stability of this material, because such lattice modulations have not been observed for SSZ-13 (built of the same structural units and having essentially the same crystallographic density as SSZ-39). However, as has been previously demonstrated by Derewinski, Barthomeuf and co-workers [29–32], the enhanced thermal stability of larger zeolite crystals compared with nanosized analogues is the consequence of the absence of high-index facets and the presence of mostly low-index facets having lower surface energy and thus increased thermal stability. It was also demonstrated that the structure of another SAPO material i.e. SAPO-37 (FAU type structure) is resistant against high temperature (up to around 900 °C) calcination [29,32]. Whereas, long-range ordering of the SAPO framework remains unchanged a solid-state transformation occurs generating new domains of different chemical composition (silicious islands and silicoaluminate domains dispersed in $AlPO_4$ matrix). It was postulated that high temperature causes the migration of T atoms (Si, Al, P) to more energetically favorable positions and this process does not lead to collapse of the framework. We cannot exclude that a similar process of Al atoms migration may occur to some extent also in SSZ-39 in this study (independently of dealumination of the framework and formation of extra framework Al species).

We also note the absence of any phosphorus in elemental mapping of both fresh and aged material, meaning that presence of P compounds (such as phosphates) occluded from SDA remnants cannot be the reason for its superior hydrothermal stability. Al dispersion remains high with no visible Al-containing aggregates in the EDS maps (note that the best EDS maps resolution is on the order of ~ nanometer). However, the NMR data clearly indicates that there are significant changes (broadening) of Al_{tetra} signal and formation of penta-coordinated Al sites as well (Fig. 6). Remarkably, H-SSZ-39 crystals survive prolonged hydrothermal aging at 900 °C and even at 1000 °C for 16 h without loss of crystallinity, but extensive modification in the environment of the Al^{3+} ions (Fig. 6). To the best of our knowledge, this is the first report showing such high hydrothermal stability of a zeolite structure after prolonged hydrothermal aging at these extreme temperatures. Surprisingly, however, we observe almost complete absence of Pd (it is present on the level of noise only) in the EDS maps of the 900 °C hydrothermally aged Pd/SSZ-39 sample. This explains that the loss of performance of this PNA material is not related to the crystal structure deterioration but to the elution of Pd from the framework at temperatures above 800 °C. At these high temperatures Pd leaves the cationic positions it originally anchored to and forms large metal particles which, in turn, can clearly be evidenced by the diffraction peak at ~40° in the XRD pattern (Fig. 7). To explain the formation of metallic palladium and not PdO it is understood that Pd(II) is eluted from the

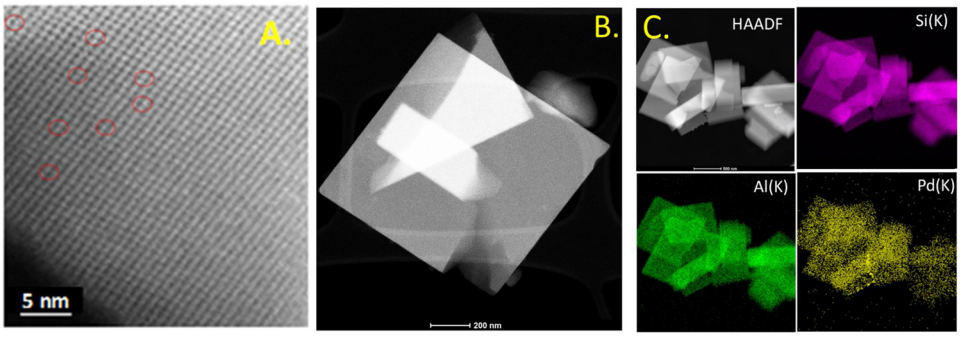

Fig. 8. A: HAADF-STEM of 0.7 wt% Pd/SSZ-39 in projection [001] (some individual Pd atoms are circled in red for clarity); B: representative image of 0.7 wt% Pd/SSZ-39 crystals with Si/Al ~ 12; C: EDS mapping of a wide area with corresponding elemental distributions. (For interpretation of the references to colour in this figure legend, the reader is referred to the web version of this article).

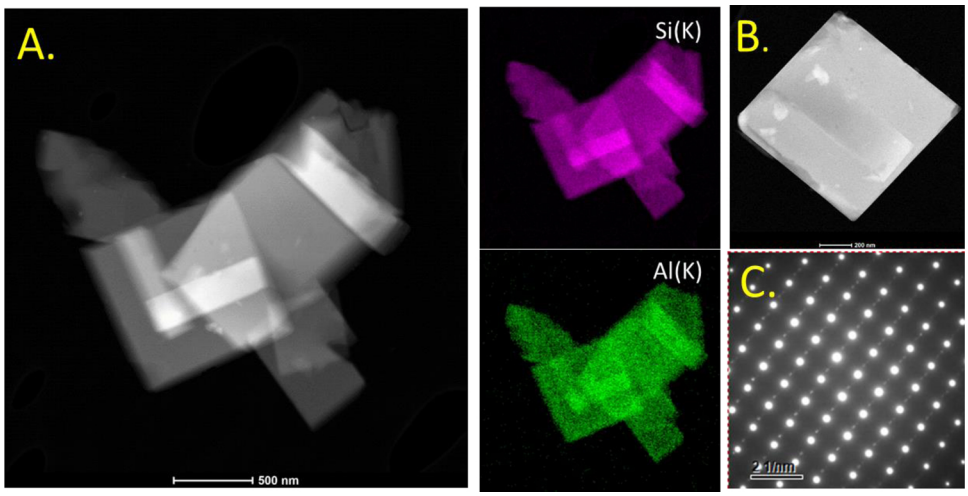

Fig. 9. HAADF-STEM of 0.7 wt% Pd/SSZ-39 after aging at 900 °C (A: large scale image with the corresponding Si and Al EDS maps; no detectable Pd signal was observed in the EDS maps and it is not shown), B: small scale image of a cubic crystal; C: XRD pattern of the crystal in B (showing highly crystalline SSZ-39 with the presence of incommensurate lattice, enlarged XRD is shown in Fig. S8).

framework as hydroxo $Pd(OH)_2$ clusters that, at these temperatures, immediately lose water to form PdO. PdO itself fully decomposes to metallic Pd at 817 °C even in the presence of 1 atm of oxygen. Although Pd/SSZ-39 under dry conditions does not lose oxygen up to above 850 °C, water promotes steam-hydrolysis with the decomposition into large Pd particles which then is unable to re-disperse in subsequent calcination. This is a very important observation, as it sets the limit of (hydro) thermal stability of Pd/Zeolite materials in the wet streams for automotive exhaust treatment applications.

3.5. Pd/SSZ-39 employed for methane combustion

Because Pd/SSZ-39 proved to be a material with outstanding hydrothermal stability, we applied it to catalytic methane combustion into carbon dioxide and water. Methane has ~25x higher impact as a greenhouse gas than carbon dioxide (the product of methane combustion), hence, it is important to abate it [33]. Pd/alumina is widely used as a catalyst for methane combustion but it is unstable in the presence of water (quickly deactivates) and its hydrothermal treatment leads to sintering of Pd into large, inactive PdO particles [34,35]. Dispersed PdO is the active phase for methane combustion, and Pd/zeolites have previously received attention as potential methane combustion materials [36–38]. We have previously described structure-Si/Al ratio relationships for fixed Pd loading on SSZ-13 with Si/Al ratios varying from 6 to 12 to 30 [8]. We showed that the increase in Si/Al ratio results in higher hydrophobicity and progressive agglomeration of PdO (and concomitant loss of isolated Pd(II) in the zeolite micropores) on the external surface with the increase of Si/Al ratio [8,11]. Olsson and co-workers produced stable Pd/SSZ-13 methane oxidation catalysts with high Si/Al ratio [36]. Because PdO is imperative for methane oxidation activity, we hypothesized that using Pd/SSZ-39 with Si/Al ~12 would provide a hydrothermally stable methane combustion material due to the high stability of the SSZ-39 framework. We prepared a 3 wt% Pd/SSZ-39 with Si/Al ~12 and applied it to methane combustion. Light-off curves for the fresh 3 wt% Pd/SSZ-39 with Si/Al ~12 are presented in Fig. 10. We used high (~ 300 L/g*hr) GHSV in the presence of water to better understand the potential to use these materials under practically relevant conditions [36]. Pd/Al_2O_3 performance (not shown for brevity) constantly deteriorates and it gets quickly inactivated in steam. The Pd/SSZ-39 material is clearly active for complete methane combustion. After hydrothermal aging at 750 °C the performance of the Pd/SSZ-39 slightly improved in the low-temperature region and modestly deteriorated in the high temperature regions. After aging at 800 °C, the Pd/SSZ-39 light-off curve shifted slightly to the right (by ~40 °C at 50 % conversion), i.e., performance degraded.

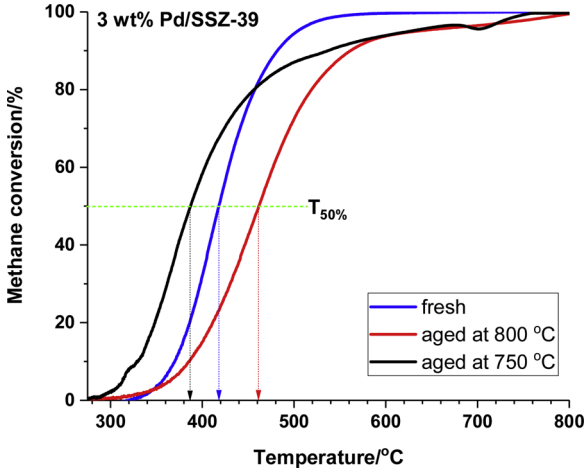

Fig. 10. Light-off curves for CH_4 combustion over 3 wt% Pd/SSZ-39 (Si/Al ~12) under the following conditions: 60 mg of catalyst, 630 ppm CH_4, 13 % O_2, 2.6 % H_2O and 5% CO_2 in nitrogen; total flow ~ 300 ml/min (GHSV ~300 L/g*hr).

We chose to test the stability and activity of the catalyst aged at 800 °C (for 16 h) at 425 °C with time on stream (Fig. S9). During the 105 h on stream test, the 800 °C-aged Pd/SSZ-39 showed stable performance. At this temperature aged Pd/SSZ-13 and Pd/Al_2O_3 show < 15 % conversion underlining the superior catalytic performance of Pd/SSZ-39 in CH_4 combustion (Figs. S12 and S13).

How can moderate deterioration of methane oxidation performance be explained after 800 °C HTA aging? The decrease in the performance may be related either to sintering of active PdO phase or re-dispersion of PdO nanoparticles to smaller entities. Therefore, we have performed HAADF-STEM imaging on 800 °C HTA (hydrothermally aged) 3 wt% Pd/SSZ-39 sample (Figs. S10,S11). In fact, low-resolution images show indeed that PdO crystals are agglomerated into large PdO nanoparticles (Fig. S10): however, few of those could be found. On the other hand, detailed high-resolution HAADF-STEM imaging of the crystals (Fig. S11) reveal the presence of extremely finely dispersed (< 1 nm) PdO species in the perfectly crystalline SSZ-13 (crystals do not deteriorate after aging at this temperature) pores and on the surface. Thus, most likely both effects (sintering and re-dispersion) contribute to the observed decrease of performance. We have previously shown [10] that if we start with atomically dispersed species for 1 wt% Pd/SSZ-13 with Si/Al ratios ~ 6 and 12, we observe formation of PdO after aging at 750 °C and elution of small amounts of Pd from the framework (the SSZ-13 framework is less stable than the framework of our SSZ-39 crystals

obviously) as PdO. However, for 1 wt% Pd/SSZ-13 with Si/Al ~ 20–30, we start with a large fraction of Pd present as PdO nanoparticles on the external surface. This particular sample after 750 ^{0}C hydrothermal aging exhibited better PNA performance as we have shown previously [10], consistent with redispersion of a fraction of PdO nanoparticles inside the more hydrophobic pores (higher Si/Al ratios of zeolite lead to more hydrophobic environments inside the pore): this high temperature hydrothermal treatment allows for some PdO to go back into the pore. It becomes clear that both processes (PdO agglomeration and PdO redispersion) may take place simultaneously under hydrothermal aging: their relative amounts depend on the framework hydrothermal stability, Si/Al ratio (hydrophobicity), temperature of aging and probably other factors.

We have also studied the effect of water in the reactant stream on the stability of CH_4 oxidation over Pd/SSZ-39. The water feed was periodically switched off to see how the sample reacts to the dry feed and then turned it back on to see if the performance restores. Unsurprisingly, we found that under dry conditions the catalytic performance was better. This is related to the fact that methane is first activated on coordinatively unsaturated Pd sites of PdO nanoparticles [47–52], followed by heterolytic cleavage of C–H bond on $Pd\delta^+$-$O^{\delta-}$ pairs. As pioneering single-crystal and DFT studies by Weaver and coworkers [53] revealed, water strongly coordinates to coordinatively unsaturated Pd sites of PdO and then dissociatively splits on Pd-O pairs with the formation tetrahedral, coordinatively saturated $Pd-OH$ moieties (with additional water molecule coordinated on the nearby Pd_1O_3 site and interacting very strongly with OH groups of $Pd-OH$ moieties). Due to formation of coordinatively saturated tetrahedral $Pd-OH$ groups, methane cannot be activated anymore on such Pd_1O_3 moieties.

However, the conversion shows a peculiar trend. Under dry conditions (after switching water off), we observed a fast (minutes) increase in methane conversion, followed by a longer time period (~16 h) was needed to stabilize the performance of the catalyst. Since we know that the zeolite structure remains robust, these changes must be associated with the water loss from the active PdO ensembles. Indeed, the simplified equilibrium: $Pd_1O_3 + H_2O \longleftrightarrow O_2Pd_1(OH)(OH)_{briding,}$ is dependent on water partial pressure. At high partial pressures of water, the equilibrium will be more shifted to the right and more Pd sites needed for methane dissociation will be covered with $-OH$ groups. As soon as water flow is stopped, water partial pressure drops and equilibrium, according to Le Chatelier's principle, shifts back to the left. However, slow return to the initial methane oxidation level indicates that at 425 ^{0}C the desorption rate of the remaining $-OH$ groups from PdO surface is slow. The trend is completely reversible and switching water off and on results basically in the same behavior. The important conclusion is that we observe a stable performance with only ~3% decrease after 105 h on stream in this case. Thus, 3 wt% Pd/SSZ-39 material with Si/Al ~ 12 represents an attractive and, more importantly, hydrothermally very stable material with potential industrial implications.

3.6. Conclusions

We showed the superior hydrothermal stability of large, uniform crystals of Pd/SSZ-39 in passive NOx adsorption, high temperature hydrothermal aging and methane combustion processes. For Pd loadings < 1 wt% the majority of Pd is present as atomically dispersed Pd (II) and $Pd(II)-OH$ species. Under PNA conditions, Pd(II)-NO, Pd(II)(OH)(NO) and Pd(II)(NO)(CO) complexes form as evidenced by FTIR data. Hydrothermal aging of SSZ-39 material does not destroy its crystal structure even at 1000 ^{0}C. Atomically dispersed Pd in Pd/SSZ-39 survives hydrothermal aging up to 815 ^{0}C, above this temperature Pd elutes from micropores forming large Pd nanoparticles probed by XRD and HAADF-STEM. Although, the crystallinity of SSZ-39 is not destroyed during aging, significant changes in Al distribution/siting are observed, with extra framework Al forming at 900 ^{0}C, as evidenced by solid state NMR measurements. Pd/SSZ-39 represents not only an attractive PNA but also an active and stable methane combustions catalyst even after prolonged hydrothermal aging at 800 ^{0}C.

CRediT authorship contribution statement

Konstantin Khivantsev: Conceptualization, Data curation, Writing - original draft. **Nicholas R. Jaegers:** Data curation. **Libor Kovarik:** Data curation. **Meng Wang:** Data curation. **Jian Zhi Hu:** Data curation. **Yong Wang:** Project administration, Supervision. **Miroslaw A. Derewinski:** Data curation, Writing - original draft. **János Szanyi:** Supervision, Writing - review & editing.

Declaration of Competing Interest

KK, MAD, JSz, NRJ, LK, YW, MW (all from PNNL) filed for a patent.

Acknowledgements

We gratefully acknowledge the U.S. Department of Energy (DOE), Energy Efficiency and Renewable Energy, Vehicle Technologies Office for the support of this work. Experiments were conducted in the Environmental Molecular Sciences Laboratory (EMSL), a national scientific user facility sponsored by the Department of Energy's Office of Biological and Environmental Research at Pacific Northwest National Laboratory (PNNL). NMR experiments were conducted in part using a Bruker 600 MHz NMR spectrometer acquired with support from the US Department of Energy, Office of Science, Office of Basic Energy Sciences (Project Number 66628). PNNL is a multi-program national laboratory operated for the DOE by Battelle Memorial Institute under Contract DE-AC06-76RL01830. M.A.D. was supported by the Materials Synthesis and Simulation Across Scales (MS3) Initiative conducted under the Laboratory Directed Research & Development Program at PNNL.

Appendix A. Supplementary data

Supplementary material related to this article can be found, in the online version, at doi:https://doi.org/10.1016/j.apcatb.2020.119449.

References

[1] J.H. Kwak, R.G. Tonkyn, D.H. Kim, J. Szanyi, C.H.F. Peden, Excellent activity and selectivity of Cu-SSZ-13 in the selective catalytic reduction of NOx with NH_3, J. Catal. 275 (2010) 187–190, https://doi.org/10.1016/j.jcat.2010.07.031.
[2] A. Beale, F. Gao, I. Lezcano-Gonzalez, C.H.F. Peden, J. Szanyi, Recent advances in automotive catalysis for NO_x emission control by small-pore microporous materials, Chem. Soc. Rev. 44 (2015) 7371–7405, https://doi.org/10.1039/C5CS00108K.
[3] R.R. Rajaram, H.-Y. Chen, D. Liu, US Patent US20150158019A1, 2015.
[4] H.-Y. Chen, J.E. Collier, D. Liu, L. Mantarosie, D. Duran-Martin, V. Novak, R. Rajaram, D. Thompsett, Low temperature NO storage of zeolite supported Pd for low temperature diesel engine emission control, Catal. Lett. 146 (2016) 1706–1711, https://doi.org/10.1007/s10562-016-1794-6.
[5] K. Khivantsev, F. Gao, L. Kovarik, Y. Wang, J. Szanyi, Molecular level understanding of how oxygen and carbon monoxide improve NOx storage in Palladium/SSZ-13 passive NOx adsorbers: the role of NO^+ and Pd(II)(CO)(NO) species, J. Phys. Chem. C 122 (2018) 10820–10827, https://doi.org/10.1021/acs.jpcc.8b01007.
[6] Y. Ji, S. Bai, M. Crocker, Al_2O_3-based Passive NOx Adsorbers for Low Temperature Applications, Appl. Catal. B Environ. 170–171 (2015) 283–292, https://doi.org/10.1016/j.apcatb.2015.01.025.
[7] S. Jones, Y. Ji, M. Crocker, CeO_2-M_2O_3, passive NOx adsorbers for cold start applications, CLEERS Workshop (2016).
[8] K. Khivantsev, N.R. Jaegers, L. Kovarik, J.C. Hanson, F.F. Tao, Y. Tang, X. Zhang, I.Z. Koleva, H.A. Aleksandrov, G.N. Vayssilov, Y. Wang, F. Gao, J. Szanyi, Achieving atomic dispersion of highly loaded transition metals in small-pore zeolite SSZ-13: high-capacity and high-efficiency low-temperature CO and passive NOx adsorbers, Angew.Chem. Int. Ed 130 (2018) 16914–16919, https://doi.org/10.1002/anie.201809343.
[9] K. Khivantsev, N.R. Jaegers, L. Kovarik, S. Prodinger, M.A. Derewinski, Y. Wang, F. Gao, J. Szanyi, Palladium/Beta zeolite passive NOx adsorbers (PNA): clarification of PNAchemistry and the effects of CO and zeolite crystallite size on PNAperformance, App.Catal. A Gen. 569 (2019) 141–148, https://doi.org/10.1016/j.apcata.2018.10.021.
[10] K. Khivantsev, N.R. Jaegers, L. Kovarik, J.Z. Hu, Y. Wang, F. Gao, J. Szanyi,

Palladium/ zeolite low temperature passive NOx adsorbers (PNA): structure-adsorption property relationships for hydrothermally aged PNA materials, Emiss. Control Sci. Technol (2019) 1–13, https://doi.org/10.1007/s40825-019-00139-w.
[11] K. Khivantsev, N.R. Jaegers, I.Z. Koleva, H.A. Aleksandrov, L. Kovarik, M. Engelhard, F. Gao, Y. Wang, G.N. Vayssilov, J. Szanyi, Stabilization of super electrophilic Pd^{+2} cations in small-pore SSZ-13 zeolite, J. Phys. Chem. C (2019), https://doi.org/10.1021/acs.jpcc.9b06760.
[12] Y. Ji, S. Bai, D. Xu, D. Qian, Z. Wu, Y. Song, R. Pace, M. Crocker, K. Wilson, A. Lee, D. Harris, D. Scapens, Pd-promoted WO_3-ZrO_2 for low temperature NOx storage, Appl.Catal. B 264 (2019) 118499, , https://doi.org/10.1016/j.apcatb.2019.118499.
[13] J.H. Kwak, J.H. Lee, S.D. Burton, A.S. Lipton, C.H.F. Peden, J. Szanyi, A common intermediate for N_2 formation in enzymes and zeolites: side-on Cu–nitrosyl complexes, Angew.Chem. Int. Ed 52 (2013) 9985–9989, https://doi.org/10.1002/anie.201303498.
[14] M. Moliner, C. Franch, E. Palomares, M. Grill, A. Corma, Cu–SSZ-39, an active and hydrothermally stable catalyst for the selective catalytic reduction of NOx, Chem. Commun 48 (2012) 8264–8266, https://doi.org/10.1039/c2cc33992g.
[15] D.L. Mowery, M.S. Graboski, T.R. Ohno, R.L. McCormick, Deactivation of PdO-Al_2O_3 oxidation catalyst in lean-bum natural gas engine exhaust: aged catalyst characterization and studies of poisoning by H_2O and SO_2, App.Catal. B 21 (1999) 157–169.
[16] I. Friberg, N. Sadokhina, L. Olsson, The effect of Si/Al ratio of zeolite supported Pd for complete CH_4 oxidation in the presence of water vapor and SO_2, App.Catal. B 250 (2019) 117–131, https://doi.org/10.1016/j.apcatb.2019.03.005.
[17] N. Martin, Z. Li, J. Martinez-Triguero, J. Yu, M. Moliner, A. Corma, Nanocrystalline SSZ-39 zeolite as an efficient catalyst for the methanol-to-olefin (MTO) process, Chem. Commun. 52 (2016) 6072–6075, https://doi.org/10.1039/c5cc09719c.
[18] R. Ranson, J. Coote, R. Moulton, F. Gao, D.F. Shantz, Synthesis and growth kinetics of zeolite SSZ-39, Ind. Eng. Chem. Res. 56 (2017) 4350–4356, https://doi.org/10.1021/acs.iecr.7b00629.
[19] D. Freude, E. Brunner, H. Pfeifer, D. Prager, H.-G. Jerschkewitz, U. Lohse, G. Oehlmann, Magic-angle-spinning NMR studies of dealuminated zeolites, Chem. Phys. Lett. 139 (1987) 325.
[20] K.I. Hadjiivanov, Identification of neutral and charged NxOy surface species by IR spectroscopy, Catal. Rev. Sci. Eng. 42 (2000) 71–144, https://doi.org/10.1081/CR-100100260.
[21] J. Szanyi, M.T. Paffett, The adsorption of NO and reaction of NO with O_2 on H-, NaH-, CuH-, and Cu-ZSM-5: an in situ FTIR investigation, J. Catal. 164 (1996) 232–245, https://doi.org/10.1006/jcat.1996.0378.
[22] K. Khivantsev, A. Vityuk, H.A. Aleksandrov, G.N. Vayssilov, D. Blom, O.S. Alexeev, M.D. Amirdis, Synthesis, modeling, and catalytic properties of HY zeolite-supported rhodium dinitrosyl complexes, ACS Catal. 7 (2017) 5965–5982, https://doi.org/10.1021/acscatal.7b00864.
[23] K. Khivantsev, A. Vityuk, H.A. Aleksandrov, G.N. Vayssilov, O.S. Alexeev, M.D. Amirdis, Effect of Si/Al ratio and Rh precursor used on the synthesis of HY zeolite-supported rhodium carbonyl hydride complexes, J. Phys. Chem. C 119 (2015) 17166–17181, https://doi.org/10.1021/acs.jpcc.5b03969.
[24] N.R. Jaegers, K.T. Mueller, Y. Wang, J.Z. Hu, Variable temperature and pressure operando MAS NMR for catalysis science and related materials, Acc. Chem. Res. 53 (2020) 611–619, https://doi.org/10.1021/acs.accounts.9b00557.
[25] N.R. Jaegers, M.Y. Hu, D.W. Hoyt, Y. Wang, J.Z. Hu, Development and application of in situ High-temperature, High-pressure magic angle spinning NMR, in: G.A. Webb (Ed.), Modern Magnetic Resonance, Springer International Publishing, Cham, 2017, pp. 1–19.
[26] N.R. Jaegers, J.K. Lai, Y. He, E. Walter, D.A. Dixon, M. Vasiliu, Y. Chen, C.M. Wang, M.Y. Hu, K.T. Mueller, I.E. Wachs, Y. Wang, J.Z. Hu, Mechanism by which tungsten oxide promotes the activity of supported V_2O_5/TiO_2 catalysts for NO_X abatement: structural effects revealed by ^{51}V MAS NMR, Angew. Chem., Int. Ed 131 (2019) 12739–12746, https://doi.org/10.1002/anie.201904503.
[27] A.G. Stepanov, Chapter 4: Basics of Solid-State NMR for Application in Zeolite Science: Material and Reaction Characterization, Zeolites and Zeolite-Like Materials, Elsevier, 2016, pp. 137–188, https://doi.org/10.1016/B978-0-444-63506-8.00004-5 ISBN 9780444635068.
[28] J. Chen, P.A. Wright, J.M. Thomas, S. Natarajan, L. Marchese, S.M. Bradley, G. Sankar, R.A. Catlow, P.L. Gai-Boyes, R.P. Townsend, M. Lok, SAPO-18 catalysts and their bronsted acid sites, J. Phys. Chem. 98 (1994) 10216–10224.
[29] M. Derewinski, M. Briend, M.J. Peltre, P.P. Man, D. Barthomeuf, Changes in the environment of silicon and aluminum in SAPO-37 zeolite during acidity measurements, J. Phys. Chem. 97 (1993) 13730–13735.
[30] M.J. Peltre, P.P. Man, M. Briend, M. Derewinski, D. Barthomeuf, Changes Upon Heating of the Distribution of Al, P and Si Atoms in the SAPO-37 Molecular Sieve, Catal.Lett. 16 (1992) 123–128.
[31] M. Derewinski, J. Jeanne Peltre, M. Briend, D. Barthomeuf, P.P. Man, Solid-state transformation of SAPO-37 molecular sieve above 1100 K, J. Chem. Soc. Faraday Trans. 89 (1993) 1823–1828.
[32] M. Briend, M.J. Peltre, P. Massiani, P.P. Man, R. Vomscheid, M. Derewinski, D. Barthomeuf, Modifications of structure and Si environment upon heating of SAPO-5, SAPO-34 and SAPO-37, Stud. Surf. Sci. Catal. 84 (1994) 613–620.
[33] K. Eguchi, H. Arai, Recent advances in high temperature catalytic combustion, Catal. Today 29 (1996) 379–386.
[34] C. Cullis, B.M. Willatt, Oxidation of methane over supported precious metal catalysts, J. Catal. 83 (1983) 267–285.
[35] N. Mouaddib, C. Feumijantou, E. Garbowski, M. Primet, Catalytic oxidation of methane over palladium supported on alumina: influence of the oxygen-to-methane ratio, Appl. Catal. A-Gen. 87 (1992) 129–144.
[36] I. Friberg, N. Sadokhina, L. Olsson, The effect of Si/Al ratio of zeolite supported Pd for complete CH_4 oxidation in the presence of water vapor and SO_2, Appl. Catal. B-Environ. 250 (2019) 117–131, https://doi.org/10.1016/j.apcatb.2019.03.005.
[37] A.K. Neyestanaki, N. Kumar, L.E. Lindfors, Catalytic combustion of propane and natural gas over Cu and Pd modified ZSM zeolite catalysts, Appl. Catal. B-Environ. 7 (1995) 95–111, https://doi.org/10.1016/0926-3373(95)00029-1.
[38] Y.J. Li, J.N. Armor, Catalytic combustion of methane over palladium exchanged zeolites, Appl. Catal. B-Environ. 3 (1994) 275–282, https://doi.org/10.1016/0926-3373(94)0006Z-H.
[39] Y.S. Ryou, J. Lee, S.J. Cho, H. Lee, C.H. Kim, D. Kim, Appl. Catal. B Environ. 212 (2017) 140–149.
[40] Y.S. Ryou, J. Lee, H. Lee, C.H. Kim, D.H. Kim, Catal. Today 320 (2019) 175–180.
[41] J. Lee, Y. Ryou, S. Hwang, Y. Kim, S.J. Cho, H. Lee, C.H. Kim, D.H. Kim, Catal. Sci. Technol. 9 (1) (2019) 163–173.
[42] J. Lee, J. Kim, Y. Kim, S. Hwang, H. Lee, C.H. Kim, D.H. Kim, Appl. Catal. B Environ. 277 (2020) 119190.
[43] K. Khivantsev, X. Wei, L. Kovarik, N.R. Jaegers, E.D. Walter, P. Tran, Y. Wang, J. Szanyi, Chemrxiv (2020), https://doi.org/10.26434/chemrxiv.12385577.
[44] K. Khivantsev, N.R. Jaegers, L. Kovarik, J. Tian, X. Isidro Pereira Hernandez, Y. Wang, J. Szanyi, Chemrxiv (2020), https://doi.org/10.26434/chemrxiv.12692264.
[45] J. Lee, Y. Ryou, S.J. Cho, H. Lee, C.H. Kim, D.H. Kim, Appl. Catal. B: Environ. 226 (2018) 71–82.
[46] E. Bello, V.J. Margarit, E.M. Gallego, F. Schuetze, C. Hengst, A. Corma, M. Moliner, Microp. Mesop. Matr. 302 (2020) 110222.
[47] N.M. Martin, M. Van den Bossche, A. Hellman, H. Gronbeck, C. Hakanoglu, J. Gustafson, S. Blomberg, N. Johansson, Z. Liu, S. Axnanda, J.F. Weaver, E. Lundgren, ACS Catal. 4 (10) (2014) 3330–3334.
[48] J.F. Weaver, J.A. Hinojosa Jr, C. Hakanoglu, A. Antony, J.M. Hawkins, A. Asthagiri, Catal. Today 160 (2011) 213.
[49] J.F. Weaver, C. Hakanoglu, A. Antony, A. Asthagiri, Chem. Soc. Rev. 43 (2014) 7536–7547.
[50] A. Antony, A. Asthagiri, J.F. Weaver, J. Chem. Phys. 139 (2013) 104702.
[51] F. Zhang, L. Pan, J. Choi, V. Mehar, J.T. Diulus, A. Asthagiri, J.F. Weaver, Angew. Chem. Int. Ed. Engl. 54 (47) (2015) 13907–13911.
[52] J.F. Weaver, C. Hakanoglu, J.M. Hawkins, A. Asthagiri, J. Chem. Phys. 132 (2010) No. 024709.
[53] H.H. Kan, R.J. Colmyer, A. Asthagiri, J.F. Weaver, J. Phys. Chem. C 113 (2009) 1495.